mathematics MDPI

Article

Computational Algorithm Based upon Dirichlet Boundary Conditions: Applications to Neutron Holograms

Ignacio Molina de la Peña [1,*], Maria L. Calvo [2] and Ramón F. Alvarez-Estrada [3]

[1] Consejo de Seguridad Nuclear, Subdirección de Ingeniería, 28040 Madrid, Spain
[2] Department of Optics, Faculty of Physics Sciences, Complutense University of Madrid, 28040 Madrid, Spain; mlcalvo@ucm.es
[3] Department of Theoretical Physics, Faculty of Physics Sciences, Complutense University of Madrid, 28040 Madrid, Spain; rfa@ucm.es
* Correspondence: imolinap@fis.ucm.es

Abstract: Neutron optics is a branch of both neutron physics and quantum physics that focuses on the study of the optical properties of slow neutrons and their dual behavior as both waves and particles. In previous research, we developed a mathematical framework based on Dirichlet boundary conditions to describe the propagation of slow neutrons in space. This approach facilitated the creation of an innovative algorithm distinguished by its computational efficiency and versatility. We applied this algorithm to the digital computation of hologram recording and reconstruction for wavelengths typical of thermal neutrons. The results demonstrate that the algorithm provides significant advantages, including rapid computation and broad applicability. It effectively handles scenarios analogous to those encountered in classical holography and shows promise for extension to other areas of physical interest.

Keywords: neutron beams propagation; Dirichlet boundary conditions; computational techniques; holography

MSC: 78M99

check for updates

Academic Editor: Didier Felbacq

Received: 1 February 2025
Revised: 16 February 2025
Accepted: 18 February 2025
Published: 24 February 2025

Citation: Molina de la Peña, I.; Calvo, M.L.; Alvarez-Estrada, R.F. Computational Algorithm Based upon Dirichlet Boundary Conditions: Applications to Neutron Holograms. *Mathematics* **2025**, *13*, 721. https://doi.org/10.3390/math13050721

1. Introduction

The mathematical formalism developed to describe the propagation of slow neutrons in space is grounded in quantum mechanics, leveraging the wave–particle duality of neutrons [1–3]. Our framework utilizes Dirichlet boundary conditions to model the interactions and constraints on the neutron wavefunction in adequate regions. The formalism incorporates the Schrödinger equation as the foundational tool to describe the evolution of the neutron wavefunction, treating neutrons as coherent wave-like entities. In a previous work, we have developed a new formalism accounting for the neutron beam propagation under confinement conditions as a zero order approximation [4]. This formalism was intended to simulate thermal neutron beams propagation phenomena as diffraction, waveguiding and interferences. Thermal neutrons are essential in applications like nuclear reactor monitoring, neutron scattering experiments, and material analysis. Briefly, the formalism is founded on Balian and Bloch's [5] approach, which involves integral equations and Green's functions for both Dirichlet and Neumann boundary conditions. Key features include: (a) wavefunction propagation: the formalism accounts for how the neutron wavefunction evolves as it interacts with potential barriers and boundaries; (b) boundary conditions: in our case, Dirichlet conditions impose specific constraints, ensuring physical solutions, such as wavefunction continuity and vanishing at specified boundaries [6]; (c) algorithmic implementation: the mathematical constructs are translated into a computational algorithm optimized for efficiency, enabling simulations of neutron wave behavior in various scenarios; and (d) applications: this formalism offers a robust framework for describing slow neutron dynamics and enables practical applications like holography by precisely modeling neutron interactions with structured media. According to the above mentioned key points, the paper is structured as follows: Section 1 is dedicated to the introduction. Section 2 (Materials and Methods) describes with details in several subsections the mathematical formulation for the wavefunction propagation and the Dirichlet boundary conditions. Section 3 (Results) consists of several subsections dedicated to the description of the algorithm and the computed digital holograms for various cases of neutron beams conditions under 2D and, eventually, 3D images and calculation of the trajectories and reconstruction. We introduce the discussion in Section 4, conclusions in Section 5, and end with the references.

2. Materials and Methods

2.1. Wavefunction Propagation

Neutron optics, applying quantum mechanics, exploits the similarities between the phenomena of neutron propagation and scattering through material media and light propagation in classical optics (which employs classical descriptions). The propagation of a slow (i.e., epithermal to ultracold) neutron beam is governed by the well-known Schrödinger's equation. If one assumes a t-independent potential for describing neutron interaction with the surrounding media, its propagation is governed by a stationary wave equation:

$$\left[-\frac{\hbar^2}{2m}\nabla^2 + V(\boldsymbol{x})\right]\phi(\boldsymbol{x}) = E\phi(\boldsymbol{x}) \tag{1}$$

In Equation (1), ϕ ($\mathbf{x}$) is a steady wavefunction for describing a slow neutron at the position $\boldsymbol{x} = (x, y, z)$, $\hbar$ is Planck's constant, m is the neutron mass (i.e., 939.57 MeV/c^2), ∇^2 is the Laplacian operator, $E = 2\pi\hbar^2/m\lambda^2{}_{\mathrm{db}}$ is the neutron total energy (λ_{db} is the neutron de Broglie wavelength): neutrons at room temperature (0.025 eV) have de Broglie wavelengths around 1.8 Å). $V(\boldsymbol{x})$ is the scattering potential. In general, $V(\boldsymbol{x})$ is the effective potential due to the nuclei in the medium. While $V(\boldsymbol{x})$ theoretically depends on $\boldsymbol{x}$, it is typically assumed to be constant for each medium in practice. This behavior is described by the well-known Fermi pseudopotential, $V = 2\pi\hbar^2 b\rho$ where ρ is the density of nuclei per unit volume, and b is the bound scattering amplitude for a slow neutron. In the most general case, b is a complex number that depends only on the mixture of isotopes, with $Im(b)$ accounting for neutron absorption. Typical potential values for common materials are in the order of $V \approx \pm 10^{-7}$ to $\pm 10^{-8}$ eV [1–3]. Equation (1) takes the form of an eigenvalue problem for the stationary wave equation, with eigenvalue E. As a result, neutron wavefunctions and probability amplitudes can describe phenomena such as reflection, refraction, interferences, and diffraction, which are central concepts studied within the field of neutron optics [7]. In what follows, and for simplicity, we will assume that no absorption take place in the considered phenomena with neutrons matter interaction.

2.2. Dirichlet Boundary Conditions

Let the scalar wavefunction $\phi(\mathbf{x})$, propagate, according to the Schrödinger equation (Equation (1)), inside the 3D unbounded domain Ω, which is partially limited by a boundary surface $\partial\Omega$ and is unbounded (extending to infinity) along a continuous set of directions. $\phi(\boldsymbol{x})$ fulfills the Dirichlet boundary conditions on $\partial\Omega$ if $\phi(\boldsymbol{x}) \to 0$, as $\boldsymbol{x}$ approaches $\partial\Omega$ from inside Ω (and so on for several $\partial\Omega_i$). In previous papers [4,6], we formulated a specific mathematical representation of the scalar function $\phi\ (\boldsymbol{x})$ using an appropriate Green's function to satisfy the Dirichlet boundary conditions for neutron beam propagation within a domain, in accordance with Equation (1). Then, a solution to Equation (1) with Dirichlet boundary conditions, $\forall \boldsymbol{x} \in \Omega$ is:

$$\phi(\boldsymbol{x}) = \phi_{in}(\boldsymbol{x}) + \sum\nolimits_{i=1}^{n} \int_{\partial\Omega_i} d\boldsymbol{x}_i' \left.\frac{\partial G\left(\boldsymbol{x}-\boldsymbol{x}_i'\right)}{\partial \boldsymbol{n}_i}\right|_{\boldsymbol{x}_i' \in \partial\Omega_i} \mu_i\left(\boldsymbol{x}_i'\right) \tag{2}$$

In Equation (2), the integrations extend over all surfaces $\partial\Omega_i$. Such boundary conditions will be reinterpreted as characterizing the form of an object, namely, the one bounded by the $\partial\Omega_i$. $\phi_{\mathrm{in}}(\boldsymbol{x})$ represents the initial neutron field entering the specified medium with wavevector $\boldsymbol{k}_{\mathbf{in}}$. It turns out that $\phi(\boldsymbol{x}) = \phi_{in}(\boldsymbol{x}) + \phi_{ts}(\boldsymbol{x})$, where $\phi_{ts}(\boldsymbol{x})$ is the truly scattered field by the medium limited by the boundary. $G(\boldsymbol{x}-\boldsymbol{x}_i')$ is the classical Green's function:

$$G\left(\boldsymbol{x}-\boldsymbol{x}_i'\right) = -\iint_{-\infty}^{+\infty} \frac{d^3\boldsymbol{K}'}{(2\pi)^3} \exp \frac{\left[i\boldsymbol{K}'\left(\boldsymbol{x}-\boldsymbol{x}_i'\right)\right]}{E + i\varepsilon - \frac{\hbar^2}{2m}\boldsymbol{K}'^2} \tag{3}$$

Its derivative is taken with respect to the unit vector $\boldsymbol{n}_{\mathbf{i}}$, representing the outward normal derivative at a generic point $\boldsymbol{x}_i'$ on the boundary surface $\partial\Omega_i$ where Dirichlet boundary conditions are imposed. $d\boldsymbol{x}_i'$ denotes the differential element (see Figure 1). The auxiliary scalar functions $\mu_i\left(\boldsymbol{x}_i'\right)$, which must be characterized, play a critical role in constructing the algorithm and applying it to specific phenomena, such as interferences and holography, in this study. One can prove that Equation (2) is a generic solution of Equation (1) for any set of auxiliary scalar functions, and that these functions take a particular form when one imposes a set of boundary conditions. The integration is defined only over the boundaries that enclose the domain, Ω. The latter may extend to infinity in certain directions. Such boundary conditions, imposed in the boundaries, $\partial\Omega_i$ characterize the form of the object.

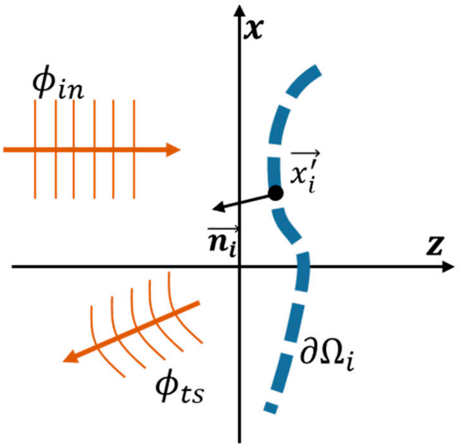

Figure 1. A schematic representation illustrates the corresponding field directions under Dirichlet boundary conditions. In the XZ plane, $\phi_{\mathrm{in}}(\boldsymbol{x})$ represents the incoming free wave. $\partial\Omega$ denotes the arbitrary boundary defining the object's geometry and extent. $\phi_{\mathrm{ts}}(\boldsymbol{x})$ is the wave truly scattered by the object at the boundary. $\boldsymbol{n}_{\mathrm{i}}$ is the outward unit vector at an arbitrary point $\boldsymbol{x}_i'$ at the boundary. Refer to Equation (2) for the corresponding mathematical formulation.

For the purpose of the forthcoming computation, it is important to note that no closed-form analytical representation can be obtained for the auxiliary functions, μ_i, $i = 1 \ldots n$. However, as stated in [4], because the Green's functions involved are locally singular at the boundaries where they are defined, the equation governing each auxiliary function depends on the incoming wavefunction, $\phi_{\mathbf{in}}$, and the other auxiliary functions, $\mu_i(\boldsymbol{x})$ (for $j = 1 \ldots n$) and $j \neq i$ but not on itself. Specifically, by imposing the Dirichlet condition, we obtain the following system of inhomogeneous linear integral equations for the density functions (compare with [6]):

$$\frac{1}{2}\frac{2m}{\hbar^2}\mu_i(\boldsymbol{x}) = -\phi_{in}(\boldsymbol{x}) - \sum_{\substack{i=1\\ i\neq j}}^{n} \int_{\partial\Omega_j} d\Omega_j \left.\frac{\partial G\left(\boldsymbol{x}-\boldsymbol{x}_j'\right)}{\partial \boldsymbol{n_j}}\right|_{\boldsymbol{x}_j'\in\partial\Omega_j} \mu_j(\boldsymbol{x}_j') \tag{4}$$

In other words:

$$\mu_i(\boldsymbol{x}) = f\left(\phi_{in}(\boldsymbol{x}), \mu_j(\boldsymbol{x})\right),\ j = 1\ldots n,\ j \neq i \tag{5}$$

By using Equations (2) and (4) (which embodies the Dirichlet boundary conditions), one obtains [4,6]:

$$\frac{2m}{\hbar^2}\frac{1}{2}\,\mu_i(\boldsymbol{x}) = -\,\phi(\boldsymbol{x})|_{x\in\partial\Omega_i} \tag{6}$$

Equation (6) shows that in order to fulfill the Dirichlet boundary conditions, the functions must be proportional to the wavefunction at the same point in the corresponding boundary line. This seems physically acceptable and is quite useful upon proceeding to our numerical iterative algorithm for the simulation of those situations that may be described by an incoming wave and a number of boundaries involving Dirichlet conditions. The terms that will arise can be interpreted as the result of the Fourier transform of the wavefunction propagating along the boundaries.

This result in Equation (6) implies that a previously computed value of the total wavefunction can be used to assign values to the auxiliary functions, enabling a step-by-step approach to their numerical characterization. Once the auxiliary functions $\mu_i(\boldsymbol{x})$ have been determined, they must be implemented into the wavefunction equation, Equation (2), to achieve the complete numerical solution.

2.3. Algorithm Implementation: Basic Characteristics

Once we had the corresponding mathematical formalism and with appropriate modifications, we found that the description of the wavefunction in Equations (2) and (6) is also suitable for numerically simulating phenomena such as neutron beam propagation, diffraction, interferences, reflected and refracted waves; we mention those as they are more significant for the purpose of our applications. In particular, one can simulate the transmittance (or reflectance) wavefunction, enabling the applications to the holographic technique.

The novelty, compared to our previous algorithm [4], lies in the redefinition of Dirichlet boundary conditions to model spatially oriented material objects on which a wave impinges and reflects. Since the neutron wave does not penetrate the boundary, the boundary itself can be regarded as an oriented object situated in free space. Once the auxiliary function, $\mu_i(\boldsymbol{x})$, corresponding to these boundaries has been determined, the truly scattered field is propagated to a specific region of space where its interaction with the incident wave is calculated, resulting in the interference pattern associated with transmittance (transmission hologram recording) or reflectance (reflection hologram recording). Both wavefunctions are automatically calculated as needed without further ado, and take Fresnel's formula into account: $R + T = 1$, where R denotes the reflectance and T the transmittance, respectively, in the absence of absorption as considered [3].

In the forthcoming section, we will introduce the foundations of holographic recording and reconstruction and the corresponding algorithmic implementation for the specific case of obtaining neutron digital holograms under various conditions.

3. Results

This section will be divided by subheadings. It will provide a concise and precise description of the holographic method foundation, the algorithm implementation, the computational results, and their interpretation, as well as the comparisons with other studies that can be drawn.

3.1. Basic Foundations of the Holographic Method

Holography is a well-known optical technique established in 1947 by Denis Gabor [8]. Initially, Gabor's primary interest lay in improving the resolution of microscopy images. However, it was later demonstrated that this new interferometric technique could store both the phase and amplitude of the light wave diffracted by an object. During the reconstruction process, the three-dimensional image of the object could be recovered, allowing for the creation of a complete holo-spatial representation.

Figure 2 presents a schematic representation of the basic setup designed by Gabor to capture an object's image. This configuration, referred to as Gabor's hologram, employs an on-line holographic arrangement. To link the scheme with the general one, as given in Figure 1, one may identify the object, (Figure 2a) located at a position $(x, 0, z)$ as a boundary $\partial\Omega_1$ on which we can define a particular point, denoted by $x_1^{'}$, and then particularizing Equation (2) for $i = 1$ and the corresponding unitary vector $\boldsymbol{n_1}$, which turns out to be parallel to the z-axis. Rays indicate direction of propagation of the thermal neutron beam energy, associated with direction of wavevector $\boldsymbol{k_{in}}$. We recall here that the slow neutron energy is defined as: $E = \left|\boldsymbol{k}_{\boldsymbol{in}}^2\right|\hbar^2/2m$ (m: mass of the neutron. $\hbar$: Planck's constant).

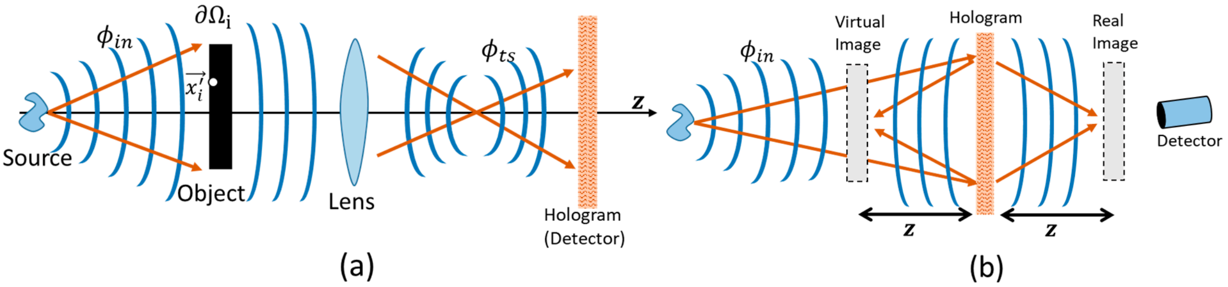

Figure 2. Graphic representation of the two steps involved in the performance of Gabor's on-line hologram: (**a**) recording, and (**b**) reconstruction. (**a**) A source emits a wavefront, ϕ_{in}, which propagates and interacts with an object (e.g., a thin slice). The diffracted (or scattered) field, ϕ_{ts}, passes through a convergent lens, resulting in a convergent beam that subsequently strikes the hologram plate (or a suitable detector). (**b**) During reconstruction, a similar source illuminates the hologram with the ϕ_{in} field. This interaction produces two twin images: a virtual image (on the left) and a real image (on the right), symmetrically positioned at a distance $\boldsymbol{z}$ from the hologram. A detector can capture these forming images. Point $\mathbf{x'}_{\mathbf{i}}\in\partial\Omega_i$.

The holographic principle was initially demonstrated entirely within the optical domain, establishing a lasting association between holography and optical fields. In the recording medium (i.e., the holographic plate), two superimposed images are captured. These twin images correspond to the virtual and real images, which become visible during the reconstruction process. The reconstruction, or reading step, involves illuminating the recorded plate with a divergent light beam generated by the optical system's illumination setup. For the interferogram to exhibit sharp definition, both interfering beams must possess a degree of mutual partial coherence, with a visibility factor near unity to ensure high-quality fringes [9]. It is noteworthy that, as illustrated in Figure 2, the use of a lens is not mandatory; its inclusion depends on the specific object and detection requirements.

It was only in 1986 when the atomic-resolution holography was introduced [10]. This approach, while also a holographic technique, differed from Gabor's method. It employed an off-axis interferometric setup, also referred to as the Leith–Upatnieks configuration [11]. Neutron holography was only later performed, in principle due to the technical requirements for using a neutron source, and a convenient detector. The first results on a neutron hologram performance were published in 2001.

The feasibility of experimental neutron holography was demonstrated in 2001 under specific conditions for the neutron beam source and extended in 2002 [12–14]. Researchers employed a technique known as the inside-detector concept. This method involves generating a point-like monochromatic source of slow neutrons within a crystal under study, which serves as a reference wave (a spherical wave). A second wave, acting as the object wave, is produced through the elastic scattering of the reference wave by single atoms within the crystal. The resulting radiation intensity distribution forms a hologram, which is typically digitized and processed for analysis. Using this technique, researchers successfully captured a hologram of a spherically shaped single quasi-crystal of $Pb_{0.9974}Cd_{0.0026}$ with a diameter of approximately 7 mm, used as the sample. In this holographic experiment, the Pb nuclei acted as the object, while the Cd nuclei functioned as point-like detectors embedded in the sample. This experiment achieved atomic-resolution determination of the quasi-crystal's structure, marking the first successful application of the neutron holographic technique for this purpose.

Nowadays, there is quite an active field of material science studies for quasi-crystal structures, for which neutron holography provides information on the internal structure of a particular object. As an example, in 2011, Klepp et al. [15] reported the use of holographically arranged grating structures behaving as mirrors for very-cold neutrons. In 2016, D. Sarenac et al. [16] obtained a spiral phase diffractive plate by means of neutron interferometry in a Mach–Zehnder type interferometer. This hologram could even be used to reconstruct neutron beams with various orbital angular momenta. Moreover, in 2017, Hayashi et al. [17] developed new experiments by using a pulsed slow neutron source. Those authors studied a Eu-doped CaF_2 single crystal and obtained a clear three-dimensional atomic image around trivalent Eu substituted for divalent Ca. The 3D real-space image was reconstructed from the theoretical holograms normalized by the 2D incident monitor pattern and by applying a convenient algorithm. Notice that the algorithm we propose in the present study may well serve for generating those 3D theoretical holograms. An advance in neutron holography was reported in 2012 by Klepp et al. [18] by using holographic gratings as efficient neutron-optical elements.

Mathematical Representation of the Holographic Process

We will describe in this subsection the mathematical formulation owing to the representation of the recording and reconstruction processes for the above-mentioned holographic technique. According to Figures 1 and 2, in which it is described the two steps, we formulate:

- Recording:

The total irradiance, I, arriving to the holographic plate (or detector) at an arbitrary point $\mathbf{x}_{\text{plate}}$ is formulated according to the classical law of interference and assuming that the process is a stationary one and, therefore, no time-dependence is considered:

$$\begin{aligned} I(\boldsymbol{x_{plate}}) &= \left\langle \left| \Psi_{ref}(\boldsymbol{x_{plate}}, t) + \Psi_{obj}(\boldsymbol{x_{plate}}, t) \right|^2 \right\rangle = \\ &= I_{ref}(\boldsymbol{x_{plate}}) + I_{obj}(\boldsymbol{x_{plate}}) + \left\langle \Psi_{ref}(\boldsymbol{x_{plate}}, t)\Psi^*_{obj}(\boldsymbol{x_{plate}}, t) \right\rangle + \left\langle \Psi^*_{ref}(\boldsymbol{x_{plate}}, t)\Psi_{obj}(\boldsymbol{x_{plate}}, t) \right\rangle \end{aligned} \tag{7}$$

where $\langle\ \rangle$ brackets denote the time average. $*$ denotes complex conjugation and I_{ref} $(\boldsymbol{x}_{\text{plate}})$ and I_{obj} $(\boldsymbol{x}_{\text{plate}})$ are the reference and object wave intensities, respectively. If we now consider the data in Figure 2, it is ready noted that:

$$\Psi_{ref}(\boldsymbol{x_{plate}}) = \phi_{in}(\boldsymbol{x_{plate}})\ ;\ \Psi_{obj}(\boldsymbol{x_{plate}}) = \phi_{ts}(\boldsymbol{x_{plate}}) \tag{8}$$

With $\phi_{in}(\boldsymbol{x_{plate}})$ and $\phi_{ts}(\boldsymbol{x_{plate}})$ as formulated in Equations (2)–(6). Moreover, in Equation (7), the first two terms on the right-hand side of the formula represent the total irradiance, from the sum of the object and reference intensities, respectively, reaching the hologram plate (or detector). In contrast, the last two terms encode the phase and amplitude information of the object, serving as key contributions to the formation of the holographic image.

- Reconstruction:

For the reconstruction process, let us assume that the recording holographic plate, or the detector used, operates under linearity conditions. Consequently, we can state that the transmittance of the recorded holographic plate, $T(\boldsymbol{x_{plate}})$, is proportional to the total irradiance reaching the plate during recording: $T(\boldsymbol{x_{plate}}) \propto I(\boldsymbol{x_{plate}})$. Furthermore, we consider that the holographic plate is illuminated with the same wavefront used during the recording, denoted as $\phi_{\text{in}}(\boldsymbol{x_{plate}})$. Then, according to Equations (2) and (7):

$$\begin{aligned} T(\boldsymbol{x_{plate}}) \quad \phi_{in}(\boldsymbol{x_{plate}}) &\propto I(\boldsymbol{x_{plate}})\phi_{in}(\boldsymbol{x_{plate}}) = |\phi(\boldsymbol{x_{plate}})|^2 \phi_{in}(\boldsymbol{x_{plate}}) \\ &= |\phi_{in}(\boldsymbol{x_{plate}})|^2 \phi_{in}(\boldsymbol{x_{plate}}) + |\phi_{ts}(\boldsymbol{x_{plate}})|^2 \phi_{in}(\boldsymbol{x_{plate}}) + |\phi_{in}(\boldsymbol{x_{plate}})|^2 \phi_{ts}(\boldsymbol{x_{plate}}) \\ &+ \phi_{in}(\boldsymbol{x_{plate}})^2 \phi_{ts}(\boldsymbol{x_{plate}})^* \end{aligned} \tag{9}$$

Thus:

$$\begin{aligned} &T(\boldsymbol{x_{plate}})\phi_{in}(\boldsymbol{x_{plate}}) \\ &\propto |\phi_{in}(\boldsymbol{x_{plate}})|^2 \phi_{in}(\boldsymbol{x_{plate}}) + \left| \sum_{i=1}^{n} \int_{\partial\Omega_i} d\boldsymbol{x}'_{\boldsymbol{i}} \left. \frac{\partial G\left(\boldsymbol{x_{plate}} - \boldsymbol{x}'_{\boldsymbol{i}}\right)}{\partial \boldsymbol{n_i}} \right|_{\boldsymbol{x}'_i \in \partial\Omega_i} \mu_i\left(\boldsymbol{x}'_{\boldsymbol{i}}\right) \right|^2 \phi_{in}(\boldsymbol{x_{plate}}) \\ &+ |\phi_{in}(\boldsymbol{x_{plate}})|^2 \left[\sum_{i=1}^{n} \int_{\partial\Omega_i} d\boldsymbol{x}'_{\boldsymbol{i}} \left. \frac{\partial G\left(\boldsymbol{x_{plate}} - \boldsymbol{x}'_{\boldsymbol{i}}\right)}{\partial \boldsymbol{n_i}} \right|_{\boldsymbol{x}'_i \in \partial\Omega_i} \mu_i\left(\boldsymbol{x}'_{\boldsymbol{i}}\right) \right] \\ &+ (\phi_{in}(\boldsymbol{x_{plate}}))^2 \left[\sum_{i=1}^{n} \int_{\partial\Omega_i} d\boldsymbol{x}'_{\boldsymbol{i}} \left. \frac{\partial G\left(\boldsymbol{x_{plate}} - \boldsymbol{x}'_{\boldsymbol{i}}\right)}{\partial \boldsymbol{n_i}} \right|_{\boldsymbol{x}'_i \in \partial\Omega_i} \mu_i\left(\boldsymbol{x}'_{\boldsymbol{i}}\right) \right]^* \end{aligned} \tag{10}$$

and, similarly, for the case of a reflection hologram, with reflectance $R = 1 - T$. Equation (10) will be the key equation at the time of implementing the algorithm as we will explain in forthcoming subsections. During reconstruction, the hologram diffracts light into multiple components, including the object wave, ϕ_{ts}, (this reconstructs the original image of the object), and the conjugate wave, $\phi^*{}_{ts}$ (this forms a virtual image that appears as a mirror-reversed or "twin" image). Both images overlap along the optical axis because the reference wave and object wave in Gabor's original setup are collinear (on-axis).

3.2. Algorithm for Holograms Simulation Based upon Dirichlet Boundary Conditions

With appropriate modifications, we found that the above description of the wavefunction, as outlined in Equations (6) and (10), can also be applied to numerically simulate the transmittance (or reflectance) function, enabling the three-dimensional reconstruction of the object (hologram). The novelty of our approach, compared to our previous algorithm [4], lies in the redefinition of Dirichlet boundary conditions to model spatially oriented material objects that interact with an incident wave, resulting in scattering. Ideally, since the neutron wave does not penetrate the boundary, the boundary itself can be conceptualized as an oriented object situated in free space (as displayed in Figure 2a). Once the shape of these boundaries, and, hence, the auxiliary functions have been calculated, ϕ_{ts} is propagated to a region of space and where its interaction with the incident wave is calculated, obtaining the interference pattern associated with the hologram.

We have also developed a methodology for the three-dimensional simulation of an object using the scattered wave function derived above. This methodology is implemented as a new model where the object transmits the incident wave based on its value, effectively simulating the hologram's reading process through diffraction propagation of the recorded pattern. These steps digitally replicate a process analogous to the recording and reading of a hologram, culminating in the encoding of the three-dimensional object as a scattered wave function. While the mathematical foundation employed shares similarities with [4,6], the development of this new numerical method and its application to a distinct field of study represents a novel contribution, to the best of our knowledge, beyond what has been previously published in this domain.

The algorithm is constituted by a total of five steps:

1. **Define an Object:**

   Identify the points $x_i' \in \partial\Omega_i$ where the objects are located.

2. **Computation of Initial Auxiliary Functions:**

   Calculate the auxiliary functions $\mu_{\mathrm{i}}\,(\mathbf{x})$ as functions of the incident wave, $\phi_{\mathrm{in}}\,(x_{\mathrm{plate}})$ using Equations (6) and (2), approximating $\phi \simeq \phi_{\mathrm{in}}$ under a first-order approximation.

3. **Scattered Wave Calculation:**

   Determine the scattered wave at points, $\boldsymbol{x_{plate}}$ where the holographic plate is defined, using Equation (2).

4. **Transmittance (or Reflectance) Calculation:**

   Evaluate the transmittance as $T(\boldsymbol{x_{plate}}) = |\phi\,(\boldsymbol{x_{plate}})|^2$; $\mathbf{x}'_{\mathrm{i}} \in \partial\Omega_{\mathrm{i}}$, considering the first order approximation used in step 2 ($\phi \simeq \phi_{\mathrm{in}}$, in Equation (6)).

5. **Hologram Reconstruction:**

   Reconstruct the hologram by applying the integral formulation $\phi_{ts}(\boldsymbol{x}) = \int_{\boldsymbol{x}_{\boldsymbol{plate}}} d\boldsymbol{x}' \frac{\partial G(\boldsymbol{x}-\boldsymbol{x}')}{\partial \boldsymbol{n}} \mu(\boldsymbol{x}')\Big|_{\boldsymbol{x}_{\boldsymbol{plate}}}$ where $\mu(\boldsymbol{x}')$ is given by $\mu(\boldsymbol{x}') = -\frac{\hbar^2}{m} T(\boldsymbol{x}')\phi_{in}(\boldsymbol{x}')$.

Regarding other specific characteristics of the algorithm, it is worth noting that the computation of the scattered wave (in step 3) and the reconstruction of the hologram (in step 5) involve Fourier transforms. This is because the Green's function used in the algorithm is represented in two dimensions as a set of all plane waves in space. For brevity, we omit further details here; see [4]. Consequently, the algorithm operates in the spatial frequency domain. Since the computation is finite, the highest spatial frequencies must be truncated. Based on our experience, spatial frequencies exceeding the spatial frequency of the incident wave ($\boldsymbol{k}_{\mathbf{in}}$) lead to evanescent waves. Thus, the upper limit for spatial frequencies can typically be defined as two to three times $|\boldsymbol{k_{in}}|$. In the following section, which presents the simulations, we will provide examples of computations for specific values of the auxiliary functions $\mu_i(\boldsymbol{x})$.

The described method offers several computational advantages: (i) it is highly flexible and not constrained by a specific mesh, (ii) it reduces the analytical problem from dealing with the entire domain to focusing only on the defined boundaries, (iii) it inherently incorporates the Sommerfeld radiation condition in the Green's functions, eliminating the need for artificial reflectionless boundaries, (iv) it allows for independent calculations at each point, facilitating straightforward parallelization, and (v) under certain conditions, it can leverage the efficiency of Fourier transforms, which naturally emerge in this formulation (utilizing the fast Fourier transform).

To the best of our knowledge, this method is novel and has not been proposed previously, leading us to have a patent granted: Ref. P202230979 [19].

3.3. Computational Simulation of Neutron Holograms

As a brief introduction, computer-generated holography, often referred to as CGH, was first introduced in 1969 by B. R. Brown and Adolph Lohmann [20]. Their innovation aimed to provide an alternative to analog holography by eliminating the need for physical objects and their associated material selection. The initial approach involved synthesizing holograms using computers to construct general optical wavefronts from numerically defined objects. Over the subsequent decades, digital holography has evolved into a routine technique for studying diverse types of holograms, with numerous applications across photonics, materials science, and industry [21]. Today, it is widely used and commercially implemented, although it is typically applied within a wavelength range different from the de Broglie wavelength utilized in this study.

However, in the wavelength domain of atomic resolution, the use of computer-generated holograms remains poorly documented. Despite exhaustive examination of the available literature, little information is available on this topic, and recent reviews lack any mention of the method [22]. We, therefore, contend that developing new computational approaches for holography at atomic resolution, including neutron holography, represents a significant and timely challenge in the field.

In this work, we focus on the regime of de Broglie wavelengths typical of neutron optics, using our approach based on Dirichlet boundary conditions. Through a computational procedure, we digitally generate holographic images of specific object shapes, corresponding to the so-called atomic resolution process.

3.3.1. The Case of Thermal Neutron Plane Waves

The simplest scenario to simulate, and test the algorithm, involves a thermal neutron beam represented as a plane wave, $\phi_{in}(\boldsymbol{x}) = e^{ik_{in}z}$, impinging on a diffractive plate. As shown in Figure 3, the plane wave is completely reflected, as expected. The diffraction contributions on the right side of the plate correspond to the diffraction from both vertices. This serves as a validation test for the implemented algorithm. Simulation details: The plate has a vertical dimension of 30 Å and is positioned at $z = 500$ Å. The incident wavefront has a de Broglie wavelength of $\lambda_{\text{db}} = 1.8$ Å, corresponding to an energy of $E = 0.025$ eV and a wavevector magnitude of $|\boldsymbol{k_{in}}| = 3.47$ Å^{-1}. The incident unit vector $\boldsymbol{n_i}$ is aligned parallel to the Z-axis. It is worth noting that the probability amplitude color bars in Figure 3 can exceed a value of 1, which is a result of interference between the reflected and incoming waves. Additionally, the algorithm is not restricted to simulating phenomena at the de Broglie wavelength; it can accommodate other wavelengths depending on the specific characteristics of the simulated phenomena.

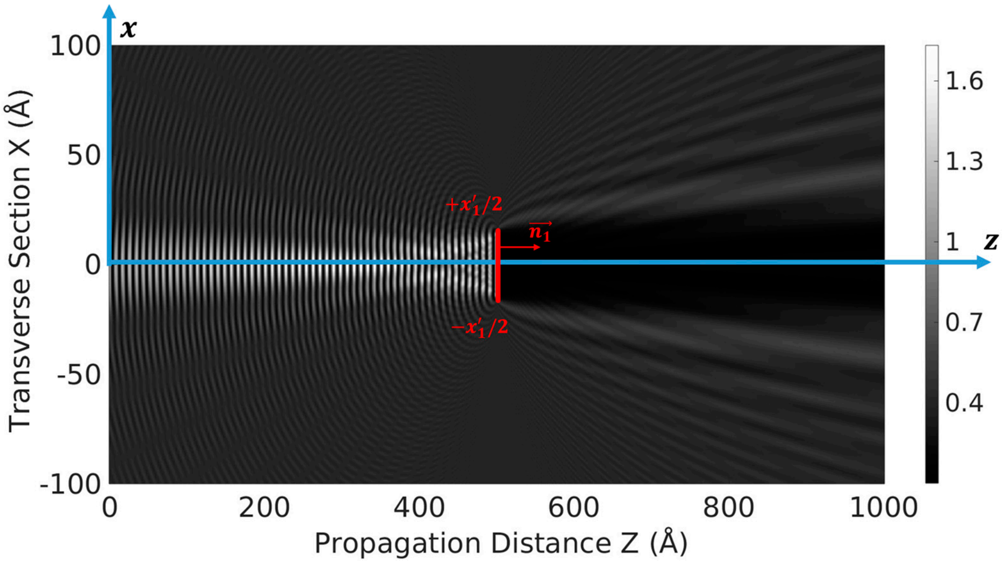

Figure 3. Simulation with the proposed algorithm of a thermal neutron beam plane wave reflected by a reflection plate. Data: Plate vertical dimension: $x_1' = 30$ Å and it is positioned at $z = 500$ Å. Wavelength of the incident thermal neutron wavefront: $\lambda_{\text{db}} = 1.8$ Å, corresponding to an energy of $E = 0.025$ eV and a wavevector magnitude of $k_{in} = 3.47$ Å^{-1}. The incident unit vector $\boldsymbol{n}_i$ is aligned parallel to the Z-axis. Gray Scale bars probability amplitudes can take values >1 due to interference of reflected wave with the incoming one.

According to Equation (2) in the particular case in Figure 3: $i = 1$. Then:

$$\phi(\boldsymbol{x}) = e^{ik_{in}z} + \int_{\partial\Omega} d\boldsymbol{x}_1' \left.\frac{\partial G\left(\boldsymbol{x} - \boldsymbol{x}_1'\right)}{\partial \boldsymbol{n}_1}\right|_{\boldsymbol{x}_1' \in \partial\Omega} \mu_1\left(\boldsymbol{x}_1'\right) \tag{11}$$

In Equation (11), the second term in the right-hand-side of the equation represents the field truly scattered by the plate and forming the simulated diffractive wavefront. Moreover, $\boldsymbol{x}_1' \equiv (x, 0, z)$. The differential area element on $\partial\Omega = \mathrm{d}^2\boldsymbol{x} = dxdz$, corresponding to a 2D simulation (see Figure 3). The simplest case for computation is to consider $\mu_1 = T(\boldsymbol{x}_1') = 1$, with $\boldsymbol{x}_1' \in \partial\Omega$.

All our simulations were performed in a personal computer laptop MSI Intel Core i5 (7th gen), Model number MS-16J9 (MSI-Netherlands, Eindhoven) with 8 GB-DDR4 RAM memory, under software MATLAB-2023b running on Linux Ubuntu 22.04, with no parallelization implemented, using one single CPU core.

Following the same operational procedure as in the preceding case, and considering the holographic recording and reading process illustrated in Figure 2, we simulated an on-line Gabor hologram with an holographic plate as the object, similar to the one shown in Figure 3. In this simulation, the holographic plate is illuminated by a plane thermal neutron wavefront. The reconstruction wavefront is identical to the one used during the recording process. For this scenario, we assumed a vertical dimension of the plate, $x_1' = 30$ Å, positioned at $z = 500$ Å, with $\lambda_{db} = 1.8$ Å.

The transmission function of the holographic plate was calculated using the conditions defined in step 4 of the algorithm, and the reconstruction procedure followed the guidelines of step 5, incorporating Equation (2). The computational representation is depicted in Figure 4, where the twin images—virtual (left) and real (right)—are correctly reproduced as expected. A neutron detector could be positioned at, for instance, $z = 1000$ Å to capture these twin images.

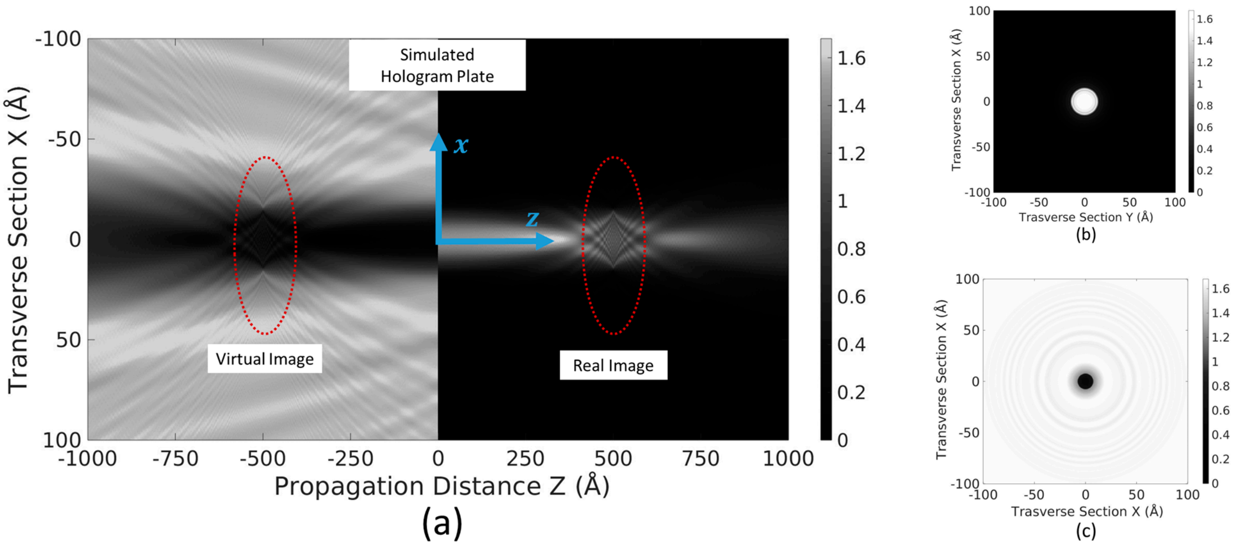

Figure 4. Reconstruction of an on-line Gabor's hologram for a vertical 30 Å plate located at $z = 500$ Å from the holographic plate. (**a**) Reconstruction of the propagation XZ field assuming the hologram is located at $z = 0$ Å. (**b**) Reconstruction of the transverse XY field at $z = 500$ Å (i.e., real image). (**c**) Reconstruction of the XY field at $z = -500$ Å (virtual image). $\phi_{in}(\mathrm{x})$ used for reconstruction is a thermal neutron ($\lambda_{db} = 1.8$ Å) plane wave with normal incidence, $\theta = 0°$. Grayscale represents probability amplitude, (values could be >1 due to interference and moiré effects). Eventually, a detector might be located at position $z = 1000$ Å in order to detect the twin images (see text for details).

There is a clear need to compare our simulation results with those of other studies. However, at present, we have not found any reports in the literature on neutron hologram simulations. This highlights the challenges associated with conducting parallel studies in this field.

To address this gap, we have compared our simulated results with available experimental data. Specifically, we reference the experimental work conducted by Sarenac et al. in 2016 [16], selecting one of their recorded holograms, as shown in Figure 5a. The object under study, Figure 5b, is a spiral-phase plate (SPP) with a topological charge of $q = 2$, a structure known to facilitate spin–orbital angular momentum exchange in a monochromatic light beam [23].

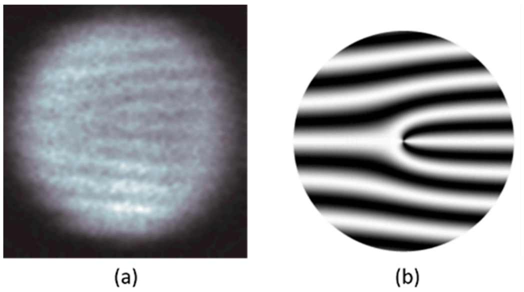

Figure 5. An example of the experimental acquisition of a neutron hologram as provided in Ref. [16]. The hologram, (**a**), is recorded using neutron interferometry with cold neutron beams. The object under investigation is a spiral-phase plate (SPP), (**b**), with topological charge $q = 2$. It is important to note that the experiment constitutes an expectation value measurement over many events, each involving a single neutron.

It is evident that the resolution of the experimental hologram is relatively low, which limits the extent of direct comparisons with the simulated results presented in Figure 4. However, an important advantage of the simulated hologram is its immunity to the intrinsic noise inherent in neutron interferometry, allowing for a clearer and more precise visualization of the holographic features.

It is pertinent to note that neutron detectors generally operate by detecting secondary reactions resulting from neutron interactions with matter, such as nuclear reactions, recoil protons, or ionization. Due to the elementary nature of neutrons, these detectors do not measure neutrons directly but rely on their interactions with specific materials such as boron, lithium-6, or helium-3. In the context of holography, the scattered radiation from individual atoms serves as the object waves, denoted in this study as $\phi_{\mathrm{ts}}(\boldsymbol{x})$, representing the true neutron scattering by the object. Real detection is performed by measuring the external diffraction pattern. However, it is worth highlighting a detection limitation: the maximum cone angle of the hologram is restricted to approximately $\pm 80^{\circ}$ due to refraction phenomena [24].

As a simple demonstration of the algorithm operative method, we show how a hologram can be located in various spatial points depending on the angle formed by the reconstruction wave (the plane wavefront in the present case). In the case of inclined beam reconstruction, the wavefront is denoted as $\phi(\boldsymbol{x}) = exp[ik(xsin\theta + zcos\theta)]$, θ: angle of incidence with respect to the z-direction and where k is the wavevector. This is then an example for off-axis procedure (not essentially Gabor's method). The computation results with this condition is displayed in Figure 6. The effect of the inclined reference beam is that the angle θ alters the propagation direction of the reconstructed wavefronts. The image is displaced due to the oblique incidence, and the vertical position of the object plate in the hologram determines the reconstructed geometry. This method is widely applied in neutron holography to analyze vertically oriented objects. It is essential for imaging applications where oblique wavefronts enhance resolution or separate overlapping features. Eventually, the detector might be located at the corresponding angle to detect the scattered field.

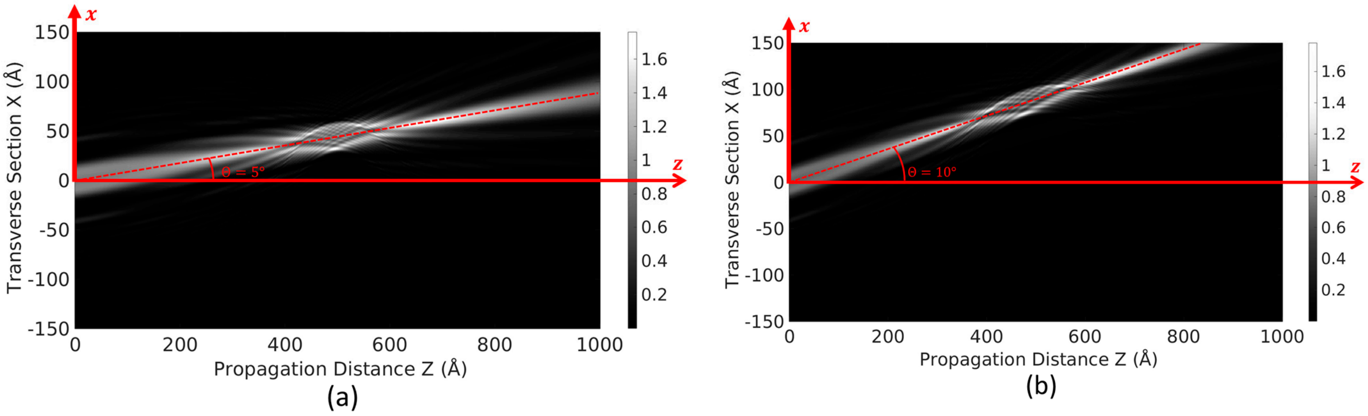

(a)

(b)

Figure 6. Reconstruction, under off-axis configuration, of a vertical 30 Å plate located at z = 500 Å for different incoming wave angles. ϕ_{in}(x) used for reconstruction is a thermal neutron (λ_{db} = 1.8 Å) plane wave with (**a**) θ_{in} = 5° and (**b**) θ_{in} = 10. Grayscale represents probability amplitude (values could be >1 due to interference and moiré effects).

3.3.2. The Case of a Non-Planar Thermal Neutron Source

In the previous computational results, we considered a perfect plane incident wave for both recording and reconstruction. From a technical perspective, in practical experiments, this implies that the neutron beam must be perfectly collimated. Thermal neutron beam collimation is crucial for ensuring spatial resolution and minimizing beam divergence in neutron scattering, imaging experiments, and holography.

Although the key methods for effective neutron beam collimation are not detailed in this paper, we refer the reader to the state-of-the-art work in this field [25]. For neutron imaging and holography, the basic requirement is to achieve a sufficiently homogeneous and well-collimated beam. This is primarily accomplished through two main techniques: (1) Pinhole collimation: This method involves using fixed apertures or pinholes made from neutron-absorbing materials, such as borated aluminum or cadmium. These apertures define the beam geometry and reduce its divergence. (2) Neutron guiding: In this approach, neutron guides minimize beam losses by reflecting neutrons within specific angular ranges, thereby reducing divergence over long distances [26].

Given the importance of these characteristics, we have extended our simulations to include scenarios where the incident and reconstruction neutron beams exhibit a non-planar geometry. For the computational purposes we have considered that the source is a faint slit or an ideal linear source. This type of sources generate cylindrical wavefronts. In particular, in neutron optics, cylindrical wavefronts can be modeled computationally for certain types of collimated beams or linear distributions of scattering sources by assuming faint neutron sources [27]. Mathematically, one function representing such a geometry is the Hankel function of first kind and zero order, then, for this particular case: $\phi_{in}(\boldsymbol{x}) = H_0^{(1)}(\boldsymbol{x})$. In the present study, the reconstruction process is performed with the same wavefront. We notice that the real part of $H_0^{(1)}(\boldsymbol{x})$ depicts oscillations, while the imaginary part accounts for the phase shift and amplitude variation. As for the expected results, cylindrical wavefronts expand outward in two dimensions, forming concentric circles around the source. The result is displayed in Figure 7.

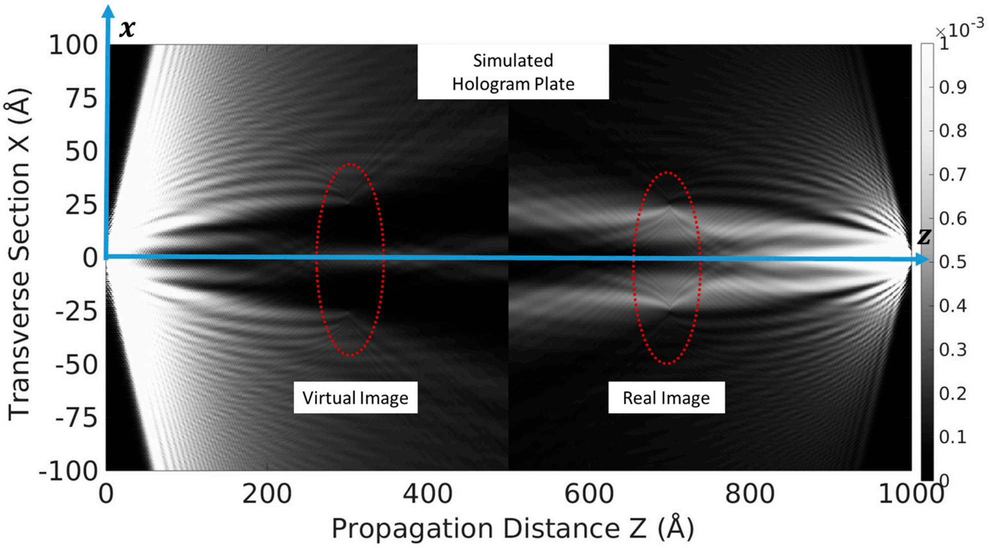

Figure 7. Simulation of the reconstruction of an on-line Gabor's hologram recorded and reconstructed with a cylindrical wavefront. Left: virtual image: z = 300 Å. Right: real image: z = 700 Å, for an object as a vertical 50 Å plate located at z = 200 Å from the digital holographic plate (located at z = 500 Å) when recording. The digital recorded hologram is located at z = 500 Å. ϕ_{in} (**x**) used for both recording and reconstruction is a thermal neutron (λ_{db} = 1.8 Å) ideal source located at z = 0, x = 0. Color bar represents probability amplitude, $|\phi\ (x)|^2$, assuming intensity distribution for the used Hankel function of first kind and zero order to be 1 (see text for details).

In Figure 7, we present the simulation results for the on-line Gabor hologram of an object: a vertically oriented 50 Å plate located at z = 500 Å and centered in the coordinate system. At the origin of coordinates (x = 0, z = 0), we place an ideal line source of a thermal neutron beam with very small dimensions (i.e., 1 Å), emitting particular non-planar waves in all directions, defined as $\phi_{in}(\boldsymbol{x}) = H_0^{(1)}(\boldsymbol{x})$, where $H_0^{(1)}(\boldsymbol{x})$ is the Hankel function of the first kind and zero order. It is worth noting that in a hypothetical 3D case, the corresponding neutron beam would approximate spherical waves, expressed as $\phi_{in}(x) = exp[ik_{in}x]/x$. The digital hologram is positioned at z = 500 Å, i.e., 200 Å away from the object.

The reconstruction process is performed using the same reference beam and assuming the normalization $\left|H_0^{(1)}(x)\right|^2 = 1$. However, it is important to highlight that, in general, $\left|H_0^{(1)}(x)\right|^2 \neq 1$. To elucidate, we briefly outline the condition applied, $\left|H_0^{(1)}(x)\right|^2 = J_0^2(x) + Y_0^2(x)$, where $J_0(x)$ is the Bessel function of the first kind and zero order, and $Y_0(x)$ is the Bessel function of the second kind (Neumann function) and zero order. The sum of these two squared functions is a variable quantity dependent on x, typically exceeding 1 for most values of x.

For computational convenience, we have normalized $|H_0^{(1)}(x)|^2$ to 1. This adjustment does not affect the overall representation of the results. The findings are consistent with those obtained in the plane wave case, serving as proof of the algorithm's consistency and robustness.

4. Discussion

The global adoption of neutron technologies for diverse applications in material science and biomedicine has led to a growing body of research demonstrating the feasibility of observing and measuring physical phenomena such as neutron beam propagation, diffraction, interference, refraction, reflection, polarization, and holography. Progress in these techniques, however, remains uneven, primarily due to the demanding infrastructure and technical support they require. Among these challenges, the technical prerequisites for specific studies, such as diffractometry and interferometry, stand out. These methods necessitate not only sophisticated experimental setups but also access to neutron sources with suitable profiles, intensity levels, operational ranges, and detection capabilities. Meeting these requirements often entails significant investments in high-cost infrastructure.

The challenges associated with research in neutron optics have prompted us to explore alternative approaches, including computational and numerical methods, in areas such as thermal neutron beam propagation, trajectory calculations, neutron waveguiding through specialized waveguides, and, more recently, holography. Our analysis of existing numerical methods in this field has revealed valuable contributions to understanding neutron beam propagation and related optical phenomena. However, we have found limited information regarding the application of holographic techniques, which are commonly employed in the study of crystals and quasicrystals within material science.

Motivated by this, we have utilized our previously developed mathematical formalism for calculating the scattered field, which is based on solutions of the Schrödinger equation through integral representations, Green's functions, and the application of Dirichlet boundary conditions. Building on this foundation, we implemented an original algorithm that incorporates this formalism alongside complementary methods, such as fast Fourier transform (FFT) calculations. The algorithm exhibits notable features, including exceptionally short computational times and remarkable flexibility to be extended from 2D to 3D representation. It can be applied to a broad range of phenomena involving neutron beam propagation, diffraction, and interference, extending beyond the constraints of de Broglie wavelengths and atomic resolution to support diverse applications.

The current development of this algorithm is particularly suited to objects with strong angular dependence in their reconstruction. While it proves useful in scenarios requiring angular filtering, our next step in its advancement focuses on enhancing surface reflection across all directions, as we are currently limited, for example, to idealized perfect mirrors or non-absorbing media. Additional promising research directions include implementing spatial frequency filtering, exploring the algorithm's behavior with sub-wavelength devices, and investigating its performance with curved geometries.

The results presented in this paper lay a solid foundation for broader future applications, which could include the incorporation of noise effects, similar to those observed in standard neutron interferometers, demonstrating that initial challenges in refining the representations can be successfully overcome. Addressing these challenges remains our primary focus for future work in this field.

5. Conclusions

In this work, we have developed an original algorithm for the implementation of digital holograms within the wavelength range of atomic-resolution imaging, with a particular focus on slow neutrons. The algorithm is based on Dirichlet boundary conditions and enables the generation of digital neutron holograms, building upon a previously patented method [19]. This approach has demonstrated the capability to reconstruct the spatial structure of predefined objects once their associated transmittance function, $T(x_{plate})$, has been calculated. The computed transmittance function encodes critical information about the object's spatial position and orientation—both in amplitude and phase—allowing for the precise generation of holograms of the target objects.

A key advantage of our method is its computational efficiency, as all calculations can be performed on a standard laptop. While our study specifically addresses neutron beams and employs the neutron wave equation, the methodology is not limited to this context. The algorithm can be readily adapted to other physical problems involving scalar wave equations, and with minimal modifications, it could be extended to three-dimensional vector wave equations, such as those describing light propagation.

Some considerations should be made on the current applicability of the algorithm. The use of Dirichlet conditions provides a robust framework that allows for efficient computation. However, note that material media exhibit, in general, a low interaction with neutrons and, thus, a certain transparency, which is not strictly the case for Dirichlet conditions. Thus, we expect that the result of the experimental implementation of these simulations would show, at least, a shape similar to that computed with a high random background (noise). Moreover, the current development of the algorithm might be less effective with the implementation of complex shapes, in which the mutual interaction of the edge effects of the shapes would play a role. In this case, the introduction of additional techniques, such as the use of spatial filters, might be necessary. The above considerations are currently awaiting further investigation.

An important consideration in neutron holography is the typically low coherence of neutron beams. We emphasize that the function $\phi(x)$ may represent either a single neutron or, in specific cases, a neutron beam. In practical neutron beam experiments, the average separation between neutrons significantly exceeds their de Broglie wavelength. As a result, the beam can be effectively regarded as an ensemble of identical quantum systems, each consisting of a single neutron prepared in the same quantum state.

We have compared our computational results with experimental neutron holograms, obtained by other authors, using a neutron interferometer [16]. Our findings indicate that digital neutron holography offers a notable advantage over experimental interferometry by mitigating resolution losses due to noise. Additionally, we propose that under certain conditions, a collection of identical scatters could be analyzed by considering a total scattering cross-section with a controllable degree of coherence. The scattering angle plays a crucial role in coherence optimization, and we expect that even low-coherence neutron beams can exhibit holographic behavior under appropriate conditions.

Future work will focus on addressing cases with high background noise through advanced quantum statistical noise reduction techniques. These developments will further enhance the applicability and robustness of neutron digital holography in experimental and theoretical settings.

6. Patents

The presented original algorithm has led to the development of a patent with the following details: Molina de la Peña, I.; Calvo, M. L.; Alvarez-Estrada, R. F.; Sistema para la generación de hologramas digitales vía simulación. [System for generating digital holograms by simulation]. *Oficina Española de Patentes y Marcas* [Spanish Patent and Trademark Office], 2023, Ref. P202230979: https://consultas2.oepm.es/pdf/ES/0000/000/02/94/08/ES-2940858_A1.pdf (see Ref. [19]).

Author Contributions: Conceptualization, M.L.C., I.M.d.l.P. and R.F.A.-E.; methodology, I.M.d.l.P., M.L.C. and R.F.A.-E.; software, I.M.d.l.P.; validation, I.M.d.l.P. and M.L.C.; formal analysis, R.F.A.-E.; investigation, M.L.C. and I.M.d.l.P.; data curation, I.M.d.l.P.; writing—original draft preparation, I.M.d.l.P. and M.L.C.; writing—review and editing; I.M.d.l.P., M.L.C. and R.F.A.-E. All authors have read and agreed to the published version of the manuscript.

Funding: This research received no external funding. One of the authors (R.F.A.-E.) is related to project with grant PID2022-136374NB-C21, funded by MCIN/AEI/10.13039/501100011033.FEDER/UE.

Data Availability Statement: The data presented in this study are available on request from the corresponding author.

Acknowledgments: I. Molina de la Peña acknowledges Belén Ramos Cid for her kind help. Authors are in debt to Flavio Bruno for his technical support.

Conflicts of Interest: The authors declare no conflicts of interest.

References

1. Bacon, G.E. *Neutron Diffraction*, 3rd ed.; Clarendon Press: Oxford, UK, 1975.
2. Sears, V.F. *Neutron Optics. An Introduction to the Theory of Neutron Optical Phenomena and their Applications*, 1st ed.; Oxford University Press: New York, NY, USA, 1989.
3. Alvarez-Estrada, R.F.; Calvo, M.L. Neutron Optics: Fundamentals. In *Advanced in Neutron Optics: Fundamentals and Applications in Materials Science and Biomedicine*; Calvo, M.L., Alvarez-Estrada, R.F., Eds.; CRC Press: Boca Raton, FL, USA, 2020; pp. 4–76.
4. Molina de la Peña, I.; Calvo, M.L.; Alvarez-Estrada, R.F. Neutron optics: New algorithm for simulating waveguides with Dirichlet boundary conditions. *Appl. Math. Mod.* **2022**, *101*, 694–715. [CrossRef]
5. Balian, R.; Bloch, C. Distribution of eigenfrequencies for wave equation in a finite domain: I. Three-dimensional problem with smoot boundary surface. *Ann. Phys.* **1979**, *60*, 401–447. [CrossRef]
6. Molina de la Peña, I.; Calvo, M.L.; Alvarez-Estrada, R.F. Neutron waveguides in neutron optics: Green's functions formalism with Dirichlet boundary conditions. *J. Mod. Opt.* **2020**, *67*, 899–913. [CrossRef]
7. Byrne, J. *Neutrons, Nuclei and Matter. An Exploration of the Physics of Slow Neutrons*; Institute of Physics Publishing: Bristol, PL, USA, 1995.
8. Gabor, D. A new microscopic principle. *Nature* **1948**, *161*, 777–778. [CrossRef] [PubMed]
9. Mandel, L.; Wolf, E. *Optical Coherence and Quantum Optics*; Cambridge University Press: Cambridge, UK, 1995; pp. 160–170.
10. Lichte, H. Electron holography approaching atomic resolution. *Ultramicroscopy* **1986**, *20*, 293–304. [CrossRef]
11. Huff, L. Holography and Holographic instruments. In *Handbook of Optics, Volume 1 Geometrical and Physical Optics, Polarized Light, Components and Instruments*, 3rd ed.; Bass, M., Ed.; Mc Graw Hill: New York, NY, USA, 2010; pp. 33.2–33.9.
12. Sur, B.; Rogge, R.B.; Hammond, R.P.; Anghel, V.N.P.; Katsaras, J. Atomic structure holography using thermal neutrons. *Nature* **2001**, *129*, 525–527. [CrossRef]
13. Cser, L.; Krexner, G.; Török, G. Atomic-resolution neutron holography. *Europhys. Lett.* **2001**, *54*, 747–752. [CrossRef]
14. Cser, L.; Török, G.; Krexner, G.; Sharkov, I.; Faragò, B. Holographic imaging of atoms using thermal neutrons. *Phys. Rev. Lett.* **2002**, *89*, 175504. [CrossRef] [PubMed]

15. Klepp, J.; Pruner, C.; Tomita, Y.; Mitsube, K.; Geltenbort, P.; Fally, M. Mirrors for slow neutrons from holographic nanoparticle-polymer free-standing film gratings. *Appl. Phys. Lett.* **2012**, *100*, 214104. [CrossRef]
16. Sarenac, D.; Huber, M.; Heacock, B.; Arif, M.; Clark, C.; Cory, D.; Shahi, C.; Pushin, D. Holography with a neutron interferometer. *Opt. Express* **2016**, *24*, 22528–22535. [CrossRef] [PubMed]
17. Hayashi, K.; Ohoyama, K.; Happo, N.; Matsushita, T.; Hosokawa, S.; Harada, M.; Inamura, Y.; Nitani, H.; Shishido, T.; Yubuta, K. Multiple-wavelength neutron holography with pulsed neutrons. *Sci. Adv.* **2017**, *3*, e1700294. [CrossRef]
18. Klepp, J.; Pruner, C.; Tomita, Y.; Geltenbort, P.; Drevensek-Olenik, I.; Gyergyek, S.; Kohlbrecher, J.; Fally, M. Holographic Gratings for Slow-Neutron Optics. *Materials* **2012**, *5*, 2788–2815. [CrossRef]
19. Molina de la Peña, I.; Calvo, M.L.; Alvarez-Estrada, R.F. Sistema para la Generación de Hologramas Digitales vía Simulación. [System for Generating Digital Holograms by Simulation]. *Oficina Española de Patentes y Marcas* [Spanish Patent and Trademark Office], 2023, Ref. P202230979. Available online: https://consultas2.oepm.es/pdf/ES/0000/000/02/94/08/ES-2940858_A1.pdf (accessed on 6 January 2025).
20. Brown, B.R.; Lohmann, A. Computer-generated Binary Holography. *IBM J. Res. Dev.* **1969**, *13*, 160–168. [CrossRef]
21. Chang, C.; Ding, X.; Wang, D.; Ren, Z.; Dai, B.; Wang, Q.; Zhuang, S.; Zhang, D. Split Lohmann computer holography: Fast generation of 3D hologram in single-step diffraction calculation. *Adv. Photonics Nexus* **2024**, *3*, 036001. [CrossRef]
22. Daimon, H.; Matsushita, T.; Matsui, F.; Hayashi, K.; Wakabayashi, Y. Recent advances in atomic resolution three-dimensional holography. *Adv. Phys X* **2024**, *9*, 1–29. [CrossRef]
23. Vaveliuk, P.; Moraes, F.; Fumeron, S.; Martinez Matos, O.; Calvo, M.L. Structure of the dielectric tensor in nematic liquid crystals with topological charge. *Opt. Lett.* **2010**, *27*, 1466–1470. [CrossRef] [PubMed]
24. Matsushita, T.; Matsui, F. Features of atomic images reconstructed from photoelectron, Auger electron, and internal detector electron holography using SPEA-MEM. *J. Electron Spectrosc. Relat Phenom.* **2014**, *195*, 365–374. [CrossRef]
25. Yu, D.; Chen, Y.; Conner, D.; Berry, K.; Skorpenske, H.; An, K. Effect of Collimation on Diffraction Signal-to-Background Ratios at a Neutron Diffractometer. *Quant. Beam Sci.* **2024**, *8*, 14. [CrossRef]
26. Ströbl, M. Neutron Imaging. In *Advanced in Neutron Optics: Fundamentals and Applications in Materials Science and Biomedicine*; Calvo, M.L., Alvarez-Estrada, R.F., Eds.; CRC Press: Boca Raton, FL, USA, 2020; pp. 177–184.
27. Klein, A.G.; Werner, S.A. Neutron Optics. *Rep. Prog. Phys.* **1983**, *46*, 259–335. [CrossRef]